Global modeling of lake-water indirect photochemistry based on the equivalent monochromatic wavelength approximation: The case of the triplet states of chromophoric dissolved organic matter

Luca Carena [a], Ángela García-Gil [b], Javier Marugán [b,*], Davide Vione [a,*]

[a] *Dipartimento di Chimica, Università di Torino, Via Pietro Giuria 5, 10125 Torino, Italy*
[b] *Department of Chemical and Environmental Technology, ESCET, Universidad Rey Juan Carlos, C/ Tulipán s/n, 28933 Móstoles, Madrid, Spain*

ABSTRACT

Chromophoric dissolved organic matter (CDOM) plays key role as photosensitizer in sunlit surface-water environments, and it is deeply involved in the photodegradation of contaminants. It has recently been shown that sunlight absorption by CDOM can be conveniently approximated based on its monochromatic absorption at 560 nm. Here we show that such an approximation allows for the assessment of CDOM photoreactions on a wide global scale and, particularly, in the latitude belt between 60°S and 60°N. Global lake databases are currently incomplete as far as water chemistry is concerned, but estimates of the content of organic matter are available. With such data it is possible to assess global steady-state concentrations of CDOM triplet states ($^3CDOM^*$), which are predicted to reach particularly high values at Nordic latitudes during summer, due to a combination of high sunlight irradiance and elevated content of organic matter. For the first time to our knowledge, we are able to model an indirect photochemistry process in inland waters around the globe. Implications are discussed for the phototransformation of a contaminant that is mainly degraded by reaction with $^3CDOM^*$ (clofibric acid, lipid regulator metabolite), and for the formation of known products on a wide geographic scale.

1. Introduction

Photochemical processes play key role in the transformation of natural compounds and anthropogenic pollutants in surface waters (Fenner et al., 2013). In particular, photoreactions are often the only important way by which biorecalcitrant compounds can be transformed in sunlit aquatic environments. These processes involve either direct photolysis or transformation by reaction with photochemically produced reactive intermediates (PPRIs) (Vione et al., 2014). PPRIs are generated by sunlight irradiation of photosensitizers such as nitrate, nitrite, and chromophoric dissolved organic matter (CDOM) (Vione et al., 2014). Main PPRIs are the hydroxyl ($^\bullet OH$) and carbonate ($CO_3^{\bullet-}$) radicals, CDOM triplet states ($^3CDOM^*$), and singlet oxygen ($^1O_2$). $^\bullet OH$ is generated by irradiation of nitrate, nitrite, and CDOM (Mack and Bolton, 1999; Niu and Croué, 2019; Sun et al., 2015), and it is mostly scavenged by dissolved organic matter (DOM, not necessarily chromophoric) (Westerhoff et al., 2007) and by inorganic carbon (HCO_3^- and CO_3^{2-}) (Wojnárovits et al., 2020). CDOM irradiation is also the source of $^3CDOM^*$, which is quenched by dissolved oxygen (McNeill and

Canonica, 2016). The latter quenching reaction gives $^1O_2$ with ~50% yield, while the main quenching process for $^1O_2$ is collision with the water solvent (Ossola et al., 2021). Finally, $CO_3^{\bullet-}$ is produced upon oxidation of HCO_3^-/CO_3^{2-} by $^\bullet OH$ (Buxton et al., 1988) and upon oxidation of CO_3^{2-} by $^3CDOM^*$ (Canonica et al., 2005). Scavenging by DOM is by far the prevailing pathway of $CO_3^{\bullet-}$ removal from surface waters (Yan et al., 2019). Although reactions with contaminants are secondary processes to consume PPRIs, they can play key role in contaminant removal (Remucal, 2014).

Photochemical generation of PPRIs in surface waters can be quantitatively assessed with light absorption calculations, by taking into account the incident spectrum of sunlight as spectral photon flux density (units of Einstein cm^{-2} s^{-1} nm^{-1}) and the absorption spectra of photosensitizers (absorbance, unitless). Considering that the spectra of both sunlight and photosensitizers are polychromatic, the relevant calculations involve numerical integrals (Vione et al., 2014). For instance, sunlight absorption by CDOM (absorbed photon flux, units of Einstein cm^{-2} s^{-1}) can be calculated as follows (Braslavsky, 2007):

$$P_{a,CDOM} = \int_{\lambda} p \circ(\lambda) \left[1 - 10^{-A_{CDOM}(\lambda)}\right] d\lambda \qquad (1)$$

where $p\circ(\lambda)$ is the spectral photon flux density of sunlight and $A_{CDOM}(\lambda)$ is the absorbance of CDOM, which is the main sunlight absorber in natural waters.

Because of the integral nature of Eq. (1) and of similar equations that account for sunlight absorption by nitrate, nitrite, and contaminants, modeling of surface-water photoreactivity is usually carried out by means of software packages (Bodrato and Vione, 2014). A recent approach has proposed a useful approximation, by which absorption of sunlight by photosensitizers can be expressed by means of monochromatic Lambert-Beer equations. The agreement between polychromatic and monochromatic equations for radiation absorption can be very good, provided that the most suitable wavelength is chosen to assess monochromatic absorption by each photosensitizer or contaminant. That is the so-called equivalent monochromatic wavelength (EMW), which is for instance 315 nm in the case of nitrate, 360 nm for nitrite, and 560 nm for CDOM (Vione, 2021). The EMW approximation allows for considerable simplification of calculation procedures in photochemical modeling, which turns out particularly useful when latitude or seasonal effects have to be considered (García-Gil et al., 2022; Vione and Carena, 2022).

An important barrier in the modeling of solar processes is the determination of accurate solar radiation doses. Since theoretical (fair-weather) solar radiation is a function of the day of the year and the latitude, only a few software tools can be found in the literature that return these values. Unfortunately, these are typically black boxes that cannot be coupled to other kinetic processes. In this context, a recent publication describes the development of a novel algorithm (Eq. (2)) to easily predict the daily dose (or cumulative irradiance, G_{day}) for different latitudes and seasons (García-Gil et al., 2022).

$$G_{day}(\lambda) = F_1 \cdot p_{sn}^{\ast}(\lambda) \cdot \tau_{DL} \qquad (2)$$

where:

- $p\circ_{sn}$ is the incident spectral photon flux density of sunlight at solar noon, which is only a function of the day of the year and latitude (units of Einstein cm^{-2} s^{-1} nm^{-1}). Briefly, the irradiance reaching the Earth's surface can be estimated only with the zenith angle for a given time and latitude (which determine the Solar Position). Once the zenith angle is defined (with expressions that only depend on the latitude and the time of the day), the relative atmospheric depth crossed by solar rays (air mass) and the radiation attenuation by the atmosphere can be calculated. Consequently, the irradiance reaching the Earth's surface is defined.
- τ_{DL} is the time from sunrise to sunset (units of s). The simple procedure to calculate it for latitudes above 60°S and below 60°N can be found in García-Gil et al. (2022). Again, only the day of the year and the latitude are required to this purpose.
- F_1 (< 1 and unitless) relates the theoretical daily dose and the hypothetical maximum cumulated incident radiation if the solar photon flux density corresponds to that at solar noon and is constant during the day length. This correction is required because the product $p\circ_{sn} \tau_{DL}$ assumes that the solar photon flux density corresponds to that at solar noon and is constant during the day, and therefore overestimates the daily dose.

Detailed calculation procedures are provided in previous work (García-Gil et al., 2022). The mentioned algorithm is not applicable to latitudes outside the 60°S-60°N belt, but within this latitude range the irradiance of sunlight is high enough to make photochemical processes important. In addition, the algorithm offers the possibility to calculate the daily dose for each wavelength. This issue is very important in the framework of the EMW approximation, because it potentially allows for

easily predicting radiation absorption and, therefore, seasonal photochemical reactions of nitrate, nitrite, and CDOM on a very wide (almost global) geographic scale.

Indirect photochemistry depends on the concentration values of water constituents, the availability of which on a worldwide scale is still insufficient. However, a novel machine-learning technique has provided an estimate of dissolved organic carbon (DOC) concentration values for many of the world's lakes (Toming et al., 2020). Although such data do not allow for an assessment of steady-state [•OH] and [CO$_3^{•-}$] values, which also require nitrate, nitrite, and inorganic carbon concentrations, they allow for a first-approximation estimate of [^{3}CDOM*] or [^{1}O$_2$]. On this basis, this work has the first goal of developing a general procedure that allows for the application of the EMW approximation to the photochemistry of CDOM on a wide geographic scale. It has also the additional goal of providing the first assessment of seasonal [^{3}CDOM*] (and hence [^{1}O$_2$], considering that [^{3}CDOM*] ~ [^{1}O$_2$] in well oxygenated waters) in the surface-water layer of global lakes that are included in the 60°S-60°N latitude belt.

2. Methods

2.1. Spectral photon flux density of sunlight as a function of month and latitude

According to the EMW approximation, sunlight absorption by CDOM can be assessed by considering monochromatic absorption at 560 nm. This wavelength was chosen because it allows for a good description of the polychromatic system by means of a much simpler monochromatic equation (Vione, 2021). The average incident spectral photon flux density of sunlight at 560 nm ($\overline{p}\circ$ (560 nm)) was defined following the easy procedure described in García-Gil et al. (2022). In that work the term F_1 has been calculated for $\lambda = 307.5$ nm, to assess the direct photoinactivation of the virus phi X174. In the present work F_1 was calculated for $\lambda = 560$ nm following an otherwise identical procedure, which enables a description of CDOM photochemistry.

Briefly, F_1 was optimized for a latitude of 45° N, considering the 15th day of each month (January-December). Optimization was carried out by minimizing the normalized root-mean-square error (NRMSE) between the values of G_{day}(560 nm) assessed with Eq. (2), and the values of the daily dose at 560 nm, under the assumption of fair-weather conditions. The latter dose values were obtained by integrating the curve that describes the photon flux density of sunlight ($p\circ$(560 nm,t)) over the time of the day (Eq. (3)). Such curve was defined with 24 points, *i.e.*, one point for each hour of the day (time step = 3600 s).

$$G_{day}(560nm) = \int_{1day} p\circ(560nm, t)\, dt \qquad (3)$$

Each value of $p\circ$(560 nm,t) was computed by introducing the zenith angle obtained with the Solar Position Algorithm (SPA) from the National Renewable Energy Laboratory (NREL) ("National Renewable Energy Laboratory, Solar Position Algorithm NREL", 2022), for each hour of the day. The same method was used to obtain $p\circ_{sn}$(560 nm) = $p\circ$ (560 nm,12 h) (García-Gil et al., 2022). In particular, $p\circ_{sn}$(560 nm) for use in Eq. (2) is expressed as follows ($\lambda = 560$ nm):

$$p\circ_{sn}(\lambda) = I_{AM0}(\lambda)$$
$$\exp\left(\frac{-\kappa(\lambda)}{\cos(\phi - \delta) + 0.506\,(96.08 + \phi - \delta)^{-1.636}}\right) \frac{\lambda}{hc} \frac{1}{N_a} \qquad (4)$$

where I_{AM0} is the intensity of sunlight outside the atmosphere, κ is the atmospheric extinction coefficient, φ is the latitude, h is Planck's constant, c is light's speed in vacuum, and N_a is Avogadro's number. Moreover, Sun's declination δ is expressed as $\delta = 23.45° \sin\left(\frac{360}{365}(day + 284)\right)$, where $day = 1$ is 1 January and $day = 365$ is 31 December. The

day length τ_{DL} (Eq. (2)) is expressed as $\tau_{DL} = \frac{2}{15} \arccos\left(-\tan(\phi)\tan(\delta)\right)$ (where the value of the arccos is in degrees and τ_{DL} in hours), which is valid for $60°S < \varphi < 60°N$ $(-60° < \varphi < 60°)$.

F_1 was then optimized by matching $G_{day}(560 \text{ nm})$ (Eq. (3)) with Eq. (2). The value of F_1 thus obtained is useful if it is valid for all relevant worldwide latitudes. To validate F_1, we computed discrete values of $G_{day}(560 \text{ nm})$ by integration of $p°(560 \text{ nm}, t)$ over the time of the day, for the 15th day of each month and in the latitude range of 60° S to 60° N, varied at steps of 5°. Such discrete, integral values were then compared with the curves expressing $G_{day}(560 \text{ nm})$ *vs.* day-of-the-year, obtained by means of Eq. (2). The degree of agreement was quantified as NRMSE.

Once the term F_1 was optimized for $\lambda = 560$ nm, the average incident spectral photon flux density of sunlight at 560 nm ($\overline{p}°(560 \text{ nm})$) was obtained by dividing Eq. (2) by the day length, τ_{DL}:

$$\overline{p}°(560nm) = F_1 \, p°_{sn}(560nm) \qquad (5)$$

The actual daily dose (for non-fair-weather conditions) can be calculated by introducing into Eq. (5) a cloud-cover factor (F_2) that relates the actual and the theoretical (fair-weather) cumulated incident radiation. The value of F_2 is variable even for the same location and day of the year since it depends on the weather conditions. Although it can be estimated based on historical data, it is strongly preferred to measure the actual irradiance in the field and calculate F_2 (by dividing the experimental value by the theoretical value). Therefore, the parameter F_2 has not been considered in this work. However, an approximation of annual average values of F_2 as a function of the latitude and longitude geocoordinates based on historical data (F_2 range: 0.5–1) can be found in García-Gil et al. (2022).

2.2. Global-scale modeling of [^{3}CDOM*]

The formation of ^{3}CDOM* stems from sunlight absorption by CDOM, and is followed by ^{3}CDOM* deactivation upon thermal processes or (prevalently) O_2 quenching (McNeill and Canonica, 2016). According to the EMW approximation, the steady-state concentration of ^{3}CDOM* is expressed as follows (note that [^{3}CDOM*] $\sim$ [$^1O_2$] in well oxygenated waters, thus the ^{3}CDOM* data can be relevant to $^1O_2$ as well):

$$[^3\text{CDOM}^*] = \frac{\varphi_{app}(^3\text{CDOM}^*) \, P_{a,\,\text{CDOM}}(560\text{nm})}{k_d} \qquad (6)$$

where $\varphi_{app}(^3\text{CDOM}^*) = 0.33$ (Vione, 2021) is the photon efficiency for ^{3}CDOM* formation from irradiated CDOM, $P_{a,\text{CDOM}}(560 \text{ nm})$ is the monochromatic photon flux absorbed by CDOM at 560 nm, and k_d is the pseudo-first order rate constant of ^{3}CDOM* quenching by O_2 in aerated solution ($k_d = 5 \times 10^5 \text{ s}^{-1}$; McNeill and Canonica, 2016). The quantum yields/quantum efficiencies of ^{3}CDOM* production by irradiated CDOM are quite variable among different CDOM types, but also the sunlight-absorbing properties of CDOM vary significantly. Actually, the inverse correlation between sunlight absorption by CDOM and ^{3}CDOM* production efficiency (Zhou et al., 2017) offsets to a certain degree the natural variations of both parameters, with the result that both ^{3}CDOM* formation rate and the steady-state [^{3}CDOM*] show lesser environmental variability than either $P_{a,\text{CDOM}}$ or $\varphi_{app}(^3\text{CDOM}^*)$ taken separately (Marchisio et al., 2015).

Because the EMW approximation considers monochromatic radiation absorption by CDOM at 560 nm, the relevant calculated absorbed photon flux is much lower than the photon flux of sunlight absorbed by CDOM at all the wavelengths. This issue is offset by the fact that $\varphi_{app}(^3\text{CDOM}^*) = 0.33$ mol Einstein^{-1} is much higher than the quantum yield of ^{3}CDOM* formation from irradiated CDOM. The value of $P_{a,\text{CDOM}}(560 \text{ nm})$ was calculated as follows (Vione, 2021):

$$\begin{aligned} &P_{a,CDOM}(560nm) \\ &= \frac{10}{d}\overline{p}°(560nm)\left[1 - 10^{-100\,A_1(560nm)\,DOC\,d}\right]^{(\alpha d^2 + \beta d + \gamma)} \end{aligned} \qquad (7)$$

where $\overline{p}°$ (560 nm) was determined with Eq. (5). Furthermore, $A_1(560 \text{ nm}) = 1 \times 10^{-4}$ L mg$_C^{-1}$ cm^{-1} is an average value for the 560-nm absorbance of CDOM, per unit DOC and optical path length of 1 cm (Vione et al., 2010). It was also assumed $d = 3$ m (*vide infra*). The exponent $\alpha d^2 + \beta d + \gamma$ has been introduced so that monochromatic absorption by CDOM could match the depth trend of polychromatic absorption, which extends over several hundreds nm. The values $\alpha = -3.0 \times 10^{-4}$ m^{-2}, $\beta = 2.2 \times 10^{-4}$ m^{-1}, and $\gamma = 0.58$ have been shown to provide an excellent match between polychromatic and monochromatic absorption, for $1\,m < d < 10$ m (Vione, 2021). Finally, 100 is the conversion factor between [m] and [cm], while 10 is the conversion factor between [cm^{-2} m^{-1}] and [L^{-1}].

By comparison, the polychromatic expression for sunlight absorption by CDOM ($P_{a,\text{CDOM}}$, units of Einstein L^{-1} s^{-1}) reads as follows (Vione, 2021):

$$P_{a,DOM} = \frac{10}{d}\int_{\lambda} p°(\lambda)\left[1 - 10^{-100\,A_1(\lambda)\,DOC\,d}\right]d\lambda \qquad (8)$$

The values of $P_{a,\text{CDOM}}(560 \text{ nm})$ (**Eq. (7)**) and $P_{a,\text{CDOM}}$ (**Eq. (8)**) are the basis for the determination of [^{3}CDOM*]. A comparison between polychromatic calculations and the EMW approximation is provided in Fig. 1. The figure shows that the EMW approach provides excellent approximation in a rather wide range of depth and DOC values, thereby simplifying calculations while entailing minimal loss in accuracy. It provides further support for the choice of 560 nm as EMW.

Considering that all other quantities are known or can be calculated, DOC is the master variable of Eq. (7). Unfortunately, a complete global database of DOC values directly measured in surface waters is not available. Remote sensing by, *e.g.*, satellites gives some possibility to assess DOC and/or CDOM, but this technique still has important limitations and can only be applied to small regions at present (Chen et al., 2020; Liu et al., 2021). In this work we used DOC data obtained by Toming et al. (2020), who employed a novel machine-learning technique and global databases to predict the DOC values in lakes with a surface area > 0.1 km^2. Input data for machine learning were catchment properties, meteorological and hydrological features, as well as lake morphometry (the latter actually played minor role in DOC variability), obtained from both WorldClim v. 2.0 23 and from HydroLAKES v. 1.0 21 databases (Toming et al., 2020).
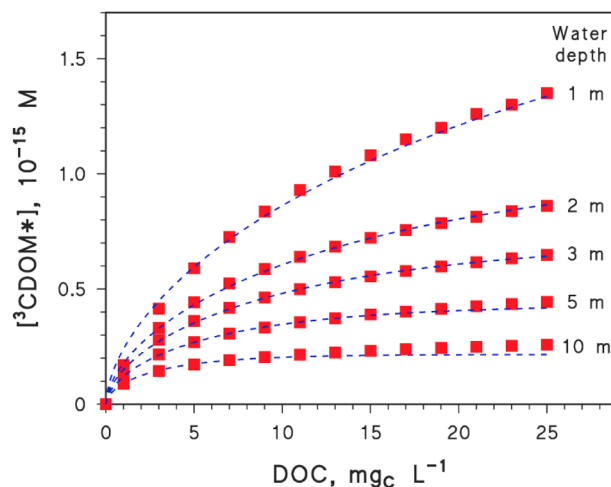

Fig. 1. Calculated steady-state [^{3}CDOM*], for different values of the water depth and the DOC. The squares represent polychromatic calculations, while the dashed curves are the assessment carried out within the EMW approximation Eqs. (6),(7), $\varphi_{app}(^3\text{CDOM}^*) = 0.33$ mol Einstein^{-1}). Sunlight irradiance data are referred to the month of April. The values of $p°(\lambda)$ and $A_1(\lambda)$ used in **Eq. (8)** are reported in *Table S1* of the Supplementary Material (**SM**). The performance of the EMW equation for $d > 10$ m is shown in *Figure S1* of the **SM**.

In particular, HydroLAKES contains data of over 1,400,000 individual lakes having surface area of at least 0.1 km^2 (Messager et al., 2016). To develop the predictive model, these databases have been used by Toming et al. (2020) together with the dataset of measured DOC values reported by Sobek et al. (2007), which consists of DOC data of ~7500 lakes mainly distributed in the boreal hemisphere.

The lake-DOC database by Toming et al. (2020) was even too large for our purposes, and some selection procedures were used to decrease the number of study lakes. First of all, lakes located above 60°N latitude were excluded because of limits connected with the calculation of $\bar{p}°(560 \text{ nm})$. Note that in the austral hemisphere, except for Antarctica, there are no continents below 60°S latitude. Moreover, although altitude is not the main factor involved in CDOM photochemistry (Zhang et al., 2020), mountain environments are characterized by higher values of UV irradiance compared to lowland ones (NCAR, 2015). For this reason, lakes located above 500 m a.s.l. were excluded from our study. This selection also allowed for reducing issues connected with winter/spring ice cover (not considered in the model), as ice cover can effectively block sunlight penetration in mountain lakes located at temperate latitudes. The surface of the lakes here selected is considered ice-free, regardless of the season. Finally, lakes having average depth lower than 5 m were also excluded to minimize problems due to sediment resuspension that can affect the DOC value in shallow lakes. The remaining 72,380 lakes had the average depth distribution shown in Table 1. The value of [^{3}CDOM*] was then calculated for a surface water layer having $d = 3$ m, for which the EMW approximation gives excellent results (see Fig. 1), and where photochemical reactions would be very important (photochemistry is most effective in the surface water layer; Vione et al., 2014). The use of a standard depth value for all lakes allows for highlighting differences related to DOC and latitude that might be of rather general validity, while both deep and shallow lakes usually occur within the same region. Furthermore, $d = 3$ m is the standard depth used in the EUSES multimedia model for regional substance risk assessments (Finch et al., 2017).

To connect the lakes with their DOC or [^{3}CDOM*] values, global mapping of the relevant quantities was carried out by means of the QGIS software (QGIS, 2020).

2.3. Model uncertainty

The DOC assessment by means of a machine-learning model entails a level of uncertainty (expressed as standard deviation, σ_{DOC}, the values of which are reported in Toming et al. (2020)), that is directly reflected into the uncertainty associated with [^{3}CDOM*], $\sigma_{^3CDOM^*}$. From Eqs. (6, 7) and the rules of error propagation, the relationship between σ_{DOC} and $\sigma_{^3CDOM^*}$ can be expressed as follows (**Text S1** in the Supplementary Material, hereinafter SM):

$$\frac{\sigma_{^3CDOM^*}}{[^3CDOM^*]} = 100 \, ln(10) \, A_1(560\text{nm}) \, d \, \left(\alpha d^2 + \beta d + \gamma\right)$$
$$\frac{10^{-100 \, A_1(560\text{nm}) \, d \, DOC}}{1 - 10^{-100 \, A_1(560\text{nm}) \, d \, DOC}} \, \sigma_{DOC} \tag{9}$$

The distributions of the relative standard deviations of both DOC and [^{3}CDOM*] are shown in Fig. 2. The relative standard deviation on the DOC (Fig. 2a) is far from negligible, but it should be considered that the DOC values ranged from < 1 to over 20 mg$_C$ L^{-1}. Therefore, distinction

between low-DOC and high-DOC environments is quite feasible despite the uncertainty.

As far as the uncertainty on [^{3}CDOM*] is concerned, the values reported in Fig. 2b are lower estimates because additional contributions other than σ_{DOC} should be considered for a proper determination of $\sigma_{^3CDOM^*}$. In particular, the following assumptions were made to describe the photochemistry of ^{3}CDOM*:

1) CDOM was considered as the main optically active component of lake water. In the presence of significant amounts of suspended solids or phytoplankton, radiation scattering by the latter would not be much of an issue. Actually, scattering would modify the underwater light field and, as a consequence, the rates of photochemical reactions as a function of water depth, but it would not change much the average reaction rates in the water column (scattering would produce higher rates at the water surface, which would be offset by lower rates in deeper layers; Calza and Vione, 2015). In contrast, sunlight absorption by suspended solids or phytoplankton would decrease both absorbed irradiance by CDOM and the steady-state [^{3}CDOM*], but that would be partially compensated by photo-activity of algal-derived organic matter (Zhang et al., 2022).

2) The connection between lake-water DOC and [^{3}CDOM*] required the use of average values of $P_{a,CDOM}(560 \text{ nm})$ and $\varphi_{app}(^3CDOM^*)$. Luckily, CDOM types having higher $P_{a,CDOM}(560 \text{ nm})$ would show lower $\varphi_{app}(^3CDOM^*)$, and *vice versa* (see Section 2.2).

3) Fair-weather sunlight irradiance was considered here (see Section 2.1).

Overall, the model values of [^{3}CDOM*] should be considered as order-of-magnitude estimates that would allow for a distinction between lakes with high or low [^{3}CDOM*].

3. Results and discussion

3.1. Optimization and validation of F_1

The first procedure was to find the value of F_1 that best matched the daily doses of radiation (integrated with Eq. (3) and calculated with Eq. (5)). To do so, the reference values of $G_{day}(560 \text{ nm})$ were calculated by 24-h integration of $p°(560 \text{ nm},t)$, for the 15th day of each month at 45°N latitude (red squares in Fig. 3). These values were the basis for optimizing F_1 with Eq. (2). The red curve in Fig. 3 shows the $G_{day}(560 \text{ nm})$ predictions with Eq. (2), using the optimized value $F_1 = 0.82$ (NRMSE = 2%).

Such a value (F_1=0.82) means that the average photon flux density of sunlight at 560 nm during the day length τ_{DL} is 82% of the photon flux density peak at the solar noon. The very good agreement shown in Fig. 3 suggests that $F_1 = 0.82$ can be used all along the year. The value of F_1 thus obtained was then validated with predictions of $G_{day}(560 \text{ nm})$, for latitudes ranging from 60°S to 60°N at 5° steps. In a similar way as for the optimization procedure, the solid symbols in Fig. 4 represent the integral of radiation intensity referred to the 15th day of each month. Conversely, curves show predictions obtained with Eq. (2) and $F_1 = 0.82$. The overall agreement was again very good, with NRMSE < 7% for all the latitude range. This finding suggests that the optimized value of F_1 can be used conveniently in the whole relevant latitude belt.

Once the algorithm was optimized and validated for $\lambda = 560$ nm, Eq. (2) could be used to obtain the values of $\bar{p}°(560 \text{ nm})$ around the world. Data for each couple of latitude-longitude values, with steps of 0.5° and for the solstices and equinoxes, can be found as a Microsoft Excel file in the **SM**.

3.2. Mapping of [^{3}CDOM*] around the globe, from 60°S to 60°N latitude

Following the selection procedure applied to the DOC database of Toming et al. (2020), the DOC map of the selected lakes is provided in
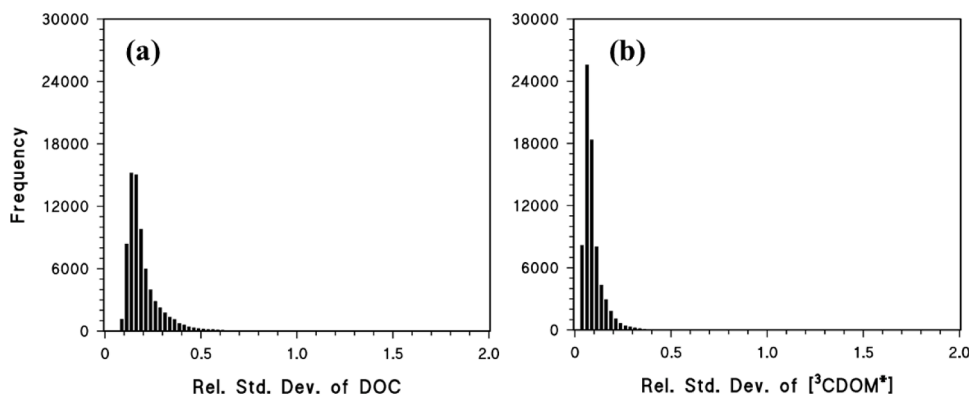
Table 1
Average depth intervals of the lakes considered in the photochemical model.

Avg. depth (d), m	Number of lakes
$5 \leq d < 10$	62,506
$10 \leq d < 25$	7703
$25 \leq d < 50$	1588
$50 \leq d < 100$	452
$d \geq 100$ ($d_{max} = 739$ m)	131

Fig. 2. Distributions of the relative standard deviations of **(a)** DOC and **(b)** [^{3}CDOM*]. The width of the frequency bars is 0.025 units of relative standard deviation.

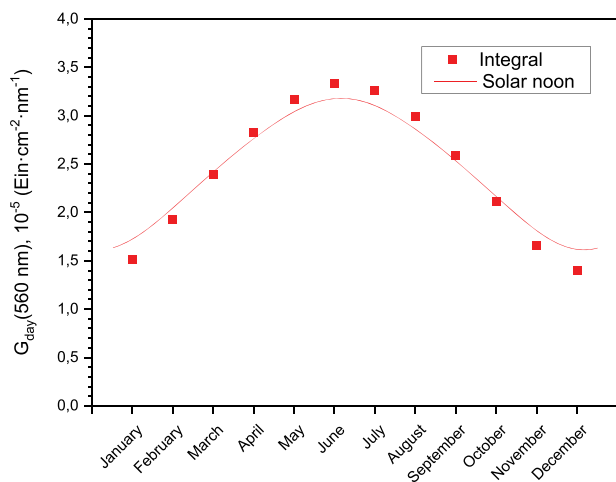**Fig. 3.** Fit for the daily dose during the year for a latitude of 45°N. The solid squares represent the values integrated along the 15th day of each month. The solid line shows the values predicted by Eq. (2), with $F_1 = 0.82$.

Fig. 5. The fact that the vast majority of the lakes is located in the temperate belt of the boreal hemisphere (30°N-60°N) is a phenomenon that does not depend on the selection procedure, except for the exclusion of the lakes located above 60°N. It is interesting to point out that the highest DOC values (> 9 mg$_C$ L^{-1}) are usually observed in Eastern Europe/Central Asia and Canada, while lakes located in the tropical belt often show moderate to low DOC levels. It is also important to observe that the latitude limits of the photochemical model exclude most of the Scandinavian peninsula, which is very rich in lakes (especially Finland) and where the DOC levels are usually very high (Toming et al., 2020).

The combination of the DOC data with the photon flux density of sunlight (Eqs. (6,7)) yielded global maps (60°S-60°N) of [^{3}CDOM*], which would also be representative of [^{1}O$_2$] values in well oxygenated waters. The [^{3}CDOM*] values thus determined are shown in Fig. 6 for summer and winter solstices (June 21st and December 21st), while the maps relative to the spring and fall equinoxes (March 20th and September 23rd) are shown in **Figure S4**.

Calculated [^{3}CDOM*] values vary in the range of $10^{-16} - 10^{-15}$ M. It is important to observe that [^{3}CDOM*] is here referred to clear-sky conditions, thereby representing the maximum steady-state concentration that can be reached in a given environment. The results shown in Figs. 6 and S4 suggest that seasonal variations of [^{3}CDOM*] generally follow the relevant variations of solar daily doses (Fig. 4). For this reason, the highest values of [^{3}CDOM*] are predicted for the temperate belt of the boreal hemisphere (30–60°N, and especially 50–60°N) during the summer solstice, while the lowest values are predicted for the same
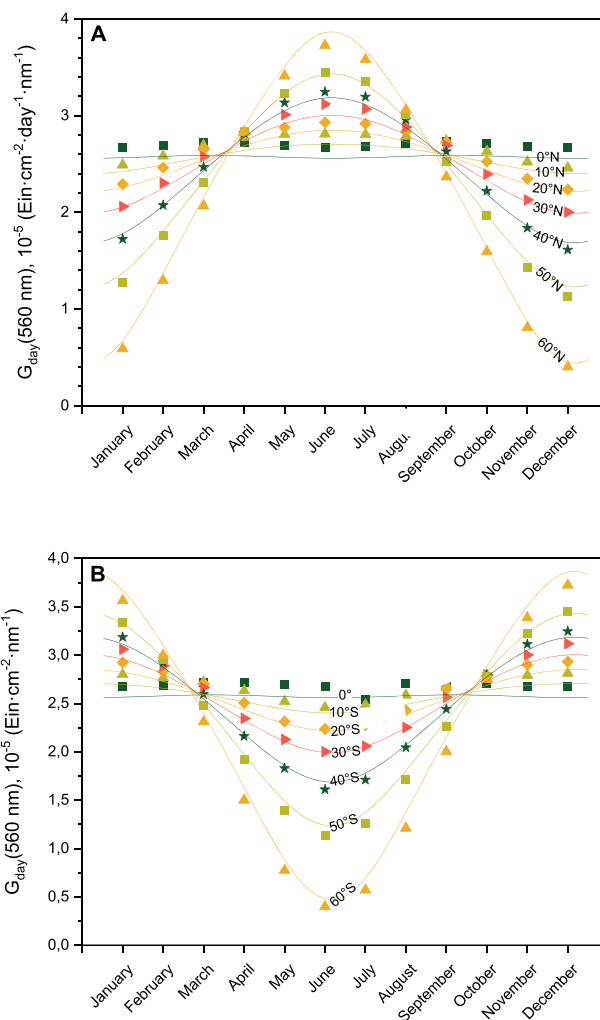

Fig. 4. Validation of the procedure to calculate the fair-weather daily dose as a function of the latitude and the day of the year (curves: calculated maximum daily dose; dots: integrated daily dose). **A:** Latitudes from 0° to 60°N with steps of 5° (shown every 10° for clarity purposes). **B:** Latitudes from 60°S to 0°.

areas during the winter solstice. The same does not happen in the southern hemisphere, partly because there is very little land (and, as a consequence, very few lakes) below 45°S, and partly because of the relatively low DOC values of lake water in these regions (Fig. 5). High water DOC in the Nordic temperate areas also explains why [^{3}CDOM*] is generally high in these regions at the equinoxes (Figure S4), while the
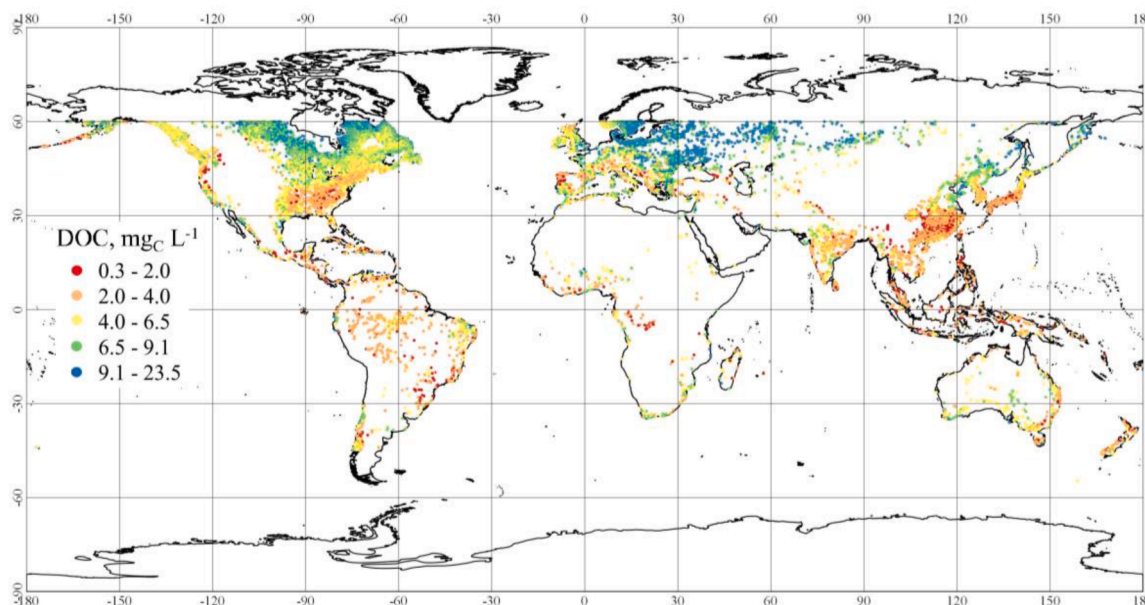
Fig. 5. DOC concentrations (mg$_C$ L^{-1}) of lakes included in the photochemical model. Data were from the work by Toming et al. (2020). Each colored dot represents a lake and does not reflect the actual lake size. To prevent readability issues of the map, dot size can be larger than the actual lake size.

560-nm daily dose does not vary as much on a global scale (Fig. 4): as shown in Fig. 1, [³CDOM*] increases with increasing DOC.

3.3. Environmental implications: photodegradation of clofibric acid

The global distribution of [³CDOM*] can, for instance, be used to assess the potential of lakes to photodegrade contaminants. On the one side, photochemical processes taking place in surface waters can depollute water bodies but, at the same time, contaminant photodegradation can sometimes produce harmful transformation products (Buth et al., 2010; Erickson et al., 2012; Halladja et al., 2007; Vogna et al., 2004).

We modeled here the photodegradation of clofibric acid (hereinafter, CLO) to show an example of how a global mapping of lake photochemistry (and, in particular, [³CDOM*]) can be used. CLO is a metabolite of blood lipid regulators, which has been widely detected in surface waters (Castiglioni et al., 2020; Korkmaz et al., 2022; Sousa et al., 2020) where it may be harmful to aquatic organisms (Coimbra et al., 2015; González-Ortegón et al., 2015). CLO is significantly transformed by photochemical reactions (Avetta et al., 2016; Carena et al., 2019; Packer et al., 2003), with major role played by ³CDOM*. Additionally, reaction with hydroxyl radicals would play secondary role (Carena et al., 2019).

An issue that should be considered in modeling CLO photodegradation is that a fraction of photooxidized CLO, here indicated as CLO•⁺ (CLO + ³CDOM* → CLO•⁺ + CDOM•⁻) can be transformed back to the parent compound by the antioxidant moieties contained in DOM (Canonica and Laubscher, 2008; Carena et al., 2019; Wenk and Canonica, 2012). Furthermore, CLO photooxidation by ³CDOM* produces both 4-chlorophenol (yield ~50%) and hydroquinone (yield ~5%), which may represent an additional concern for aquatic ecosystems (Avetta et al., 2016).

Figs. 7 and S5 show the global mapping of the photochemical half-life time ($t_{1/2}$) of CLO, as accounted for by its main reaction with ³CDOM*. That depicted here is clearly a somewhat fictitious scenario because it assumes that CLO occurs in all the studied lakes, which is fortunately not the case. However, it gives insight into the vulnerability of different lake environments to the potential occurrence of CLO.

The half-life time $t_{1/2}$ was calculated as per Eq.(10), where $k_{3CDOM*+CLO} = 5.2 \times 10^9$ L mol^{-1} s^{-1} (Carena et al., 2019), τ_{DL} is the day

length (units of h day^{-1}) computed as above, and $\psi = 0.68 + 0.32 (1 + 10\,DOC)^{-1}$ is a parameter that takes into account the back-reactions of photooxidized CLO with antioxidant DOM moieties (for details, see Carena et al., 2019).

$$t_{1/2} = \frac{ln\,2}{3600\,\psi\,k_{3CDOM*+CLO}\,[^3CDOM*]\,\tau_{DL}} \quad (10)$$

Despite the fact that ψ decreases as the DOC increases (meaning that ψ also decreases as [³CDOM*] increases, because of the proportionality between [³CDOM*] and the DOC, see Fig. 1), the value of $t_{1/2}$ decreases with increasing [³CDOM*].

The obtained results allow for a rough comparison between the predicted photodegradation kinetics and the disappearance of CLO in the field. A previous study has reported an upper limit for the photodegradation kinetics of CLO as $k' \leq 0.01$ day^{-1} in the epilimnion of lake Greinfensee (Switzerland) in late summer (depth of the thermocline ~ 10 m; note that Greinfensee is ~ 30 m deep: Tixier et al., 2003). With our model, we obtained $k' \sim 0.08$ day^{-1} in the Greifensee for a water column with depth $d = 3$ m on fall equinox. This value has to be corrected for common mid-latitude irradiance, which is ~ 1.5 times lower compared to a clear-sky scenario (Frank and Klöpffer, 1988), and for the different water depths (10 m vs. 3 m), obtaining $k' \sim 0.02$ day^{-1}. This result is not so far from that assessed in the field if one considers all the approximations used in our model. Note that a two-times difference can be also found between the values of [³CDOM*] obtained here and those assessed in a previous study. Canonica et al. (1995) reported in fact [³CDOM*] ~ 10^{-14} mol L^{-1} for the top 1-m of lake Greinfensee under summer-noon sunlight, which would mean ~ 10^{-15} mol L^{-1} if one considers the entire 10-m epilimnion. Under the same conditions we predict [³CDOM*] ~ 5.5 × 10^{-16} mol L^{-1}.

The $t_{1/2}$ values of CLO follow those of [³CDOM*] (the highest [³CDOM*], the lowest $t_{1/2}$, see Figs. 6 and 7, and the maps for the equinoxes in the **SM**). In most cases, CLO lifetimes range within 4–16 days. However, the highest seasonal variability is predicted for the temperate areas of the northern hemisphere, and especially the 50–60°N latitude belt. In that region, the calculated values of $t_{1/2}$ range from 3 to 4 days at the summer solstice to 16–67 days at the winter solstice. The same does not happen in the corresponding region of the southern hemisphere, mainly due to scarcity of land and, therefore, lakes. Furthermore, the few lakes located in that region of the southern

6
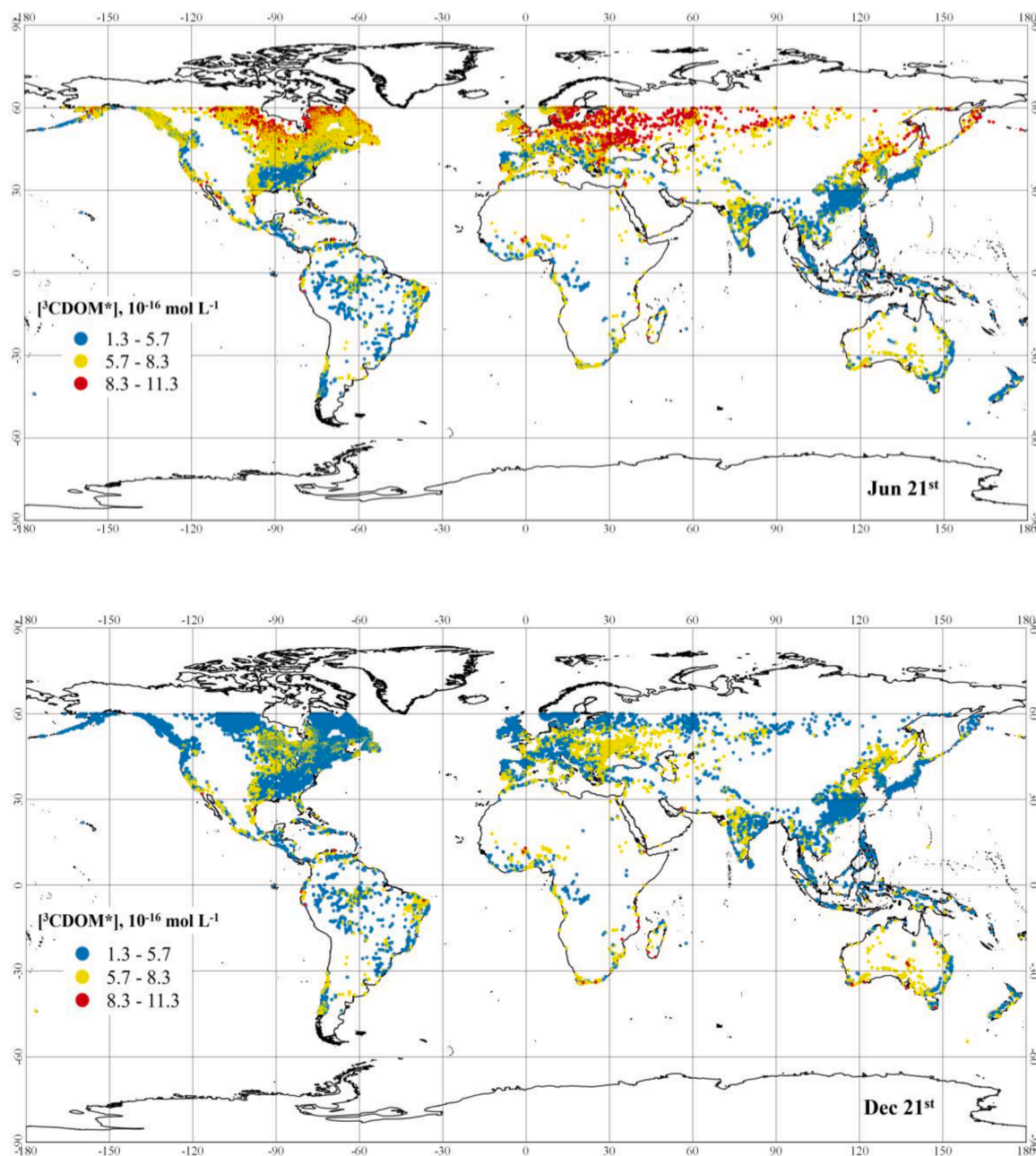
Fig. 6. Global maps of the steady-state [^{3}CDOM*] (units of 10^{-16} mol L^{-1}) for solstices (June 21st and December 21st), assessed for a 3 m-deep water column under clear-sky conditions. Each colored dot represents a lake and does not reflect the actual lake size. To prevent readability issues of the map, dot size can be larger than the actual lake size.

hemisphere have relatively low DOC, which would prevent [^{3}CDOM*] from reaching high values in December and, therefore, would also prevent $t_{1/2}$ from being proportionally low.

As mentioned before, CLO photodegradation gives both 4-chlorophenol (ClPhOH) with yield $\eta_{ClPhOH} \sim 0.5$, and hydroquinone (HQ) with $\eta_{HQ} \sim 0.05$ (Avetta et al., 2016). The rate coefficient of ClPhOH photoformation, $k'_{f,ClPhOH}$ (day^{-1} units), is obtained from the rate constant of CLO photodegradation ($k_{CLO} = \ln 2 \ (t_{1/2})^{-1} = 3600 \ \psi \ k_{^3CDOM^*+CLO} \ [^3CDOM^*] \ \tau_{DL}$), as $k'_{f,ClPhOH} = \eta_{ClPhOH} \ k_{CLO} = 3600 \ \eta_{ClPhOH} \ \psi \ k_{^3CDOM^*+CLO} \ [^3CDOM^*] \ \tau_{DL}$. The corresponding rate coefficient for HQ is $k'_{f,HQ} = 0.1 \ k'_{f,ClPhOH}$, because $\eta_{HQ} = 0.1 \ \eta_{ClPhOH}$. The global ($60°S < \varphi < 60°N$) maps of $k'_{f,ClPhOH}$, which are also indicative of $k'_{f,HQ}$, are shown in **Figure S6 (SM)**. The values of $k'_{f,ClPhOH}$ are highest in the temperate areas of the northern hemisphere at the summer solstice, and lowest in the same areas at the winter solstice. The tropical belt and the southern

hemisphere show intermediate values of $k'_{f,ClPhOH}$. Interestingly, ClPhOH formation in the spring and fall equinoxes is consistently lower in Southern China, Southern Japan, and the South-Eastern US compared with other locations at comparable latitude (**Figure S6 (SM)**). The most likely explanation lies in the relatively low DOC values of the relevant lakes (see Fig. 5).

Photochemical mapping as per this work can support (and, potentially, be integrated into) ecotoxicological risk assessment (ERA), in order to see if photochemical reactions taking place in surface waters can act as real self-depollution processes for water bodies, or if the production of by-products upon pollutant photodegradation can increase the ecological risk. **Text S2** describes how the risk quotient (RQ) of a contaminant, which is a parameter commonly used in ERA studies to determine the ecological risk (Gosset et al., 2021; Topaz et al., 2020; Wielens Becker et al., 2020), can be expressed as a function of
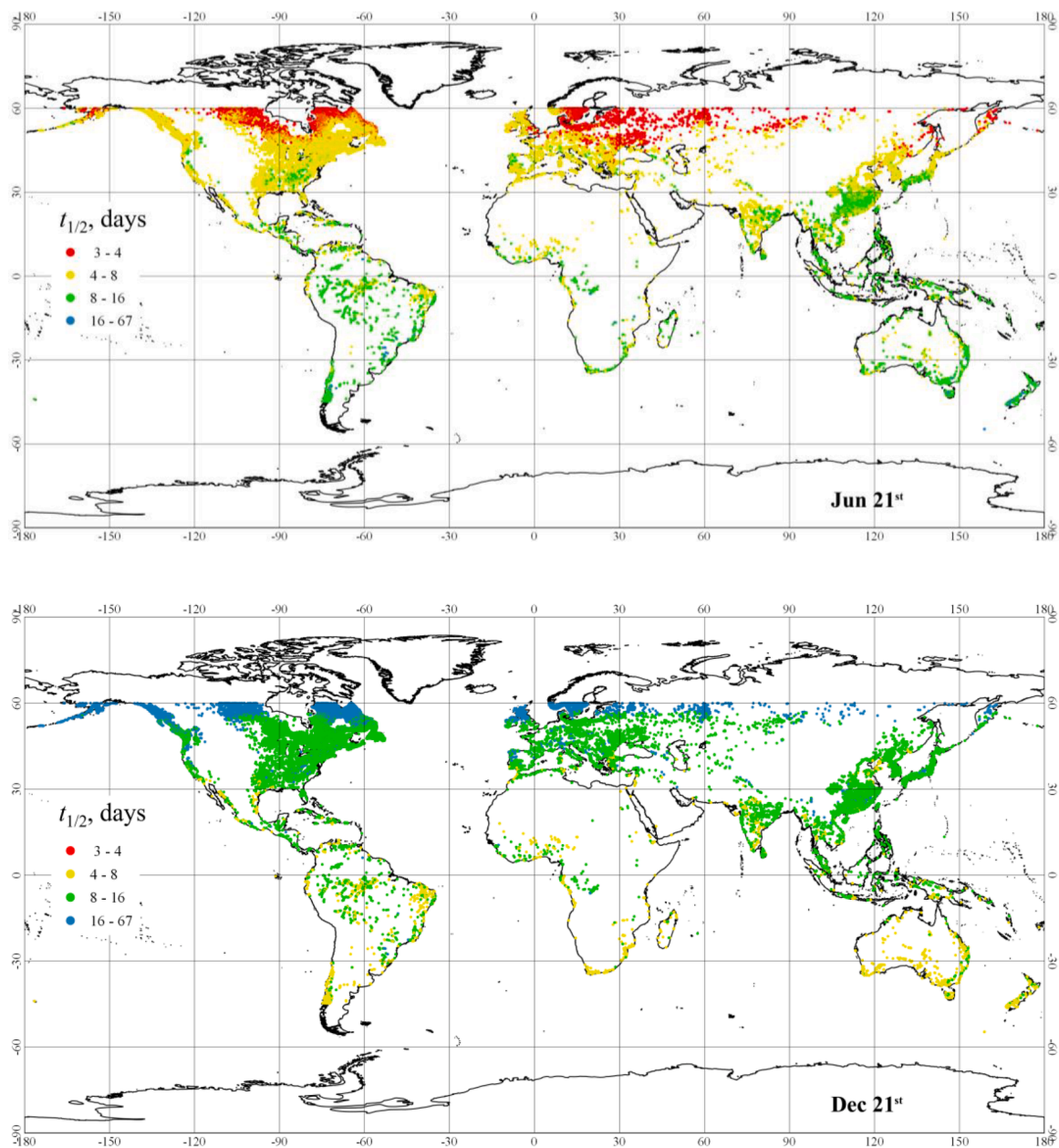
Fig. 7. Global maps of the half-life time (day units) of CLO accounted for by its photoreactions with ³CDOM*. The maps are referred to solstices, under clear-sky conditions, and to water depth $d = 3$ m. Each colored dot represents a lake and does not reflect the actual lake size. To prevent readability issues of the map, dot size can be larger than the actual lake size.

parameters describing pollutant photodegradation. In a simplified scenario where the photodegradation of ClPhOH and HQ into different transformation products was neglected (which is reasonable when considering the evolution of CLO, ClPhOH, and HQ between sunrise and sunset in a single day; Avetta et al., 2016), it could be seen that CLO reaction with ³CDOM* would actually increase the ecological risk, and the increase would be higher where the transformation of CLO is faster. The reason is the higher toxicity for aquatic organisms of both ClPhOH and HQ, compared to CLO.

4. Conclusions

- By applying the EMW approximation to the absorption of sunlight by CDOM, it is possible to approximately predict the steady-state [³CDOM*] on the basis of the photon flux density of sunlight at 560 nm and of water DOC values. The average daily photon flux

density can be expressed as $\bar{p}_\circ(560nm) = F_1\, p^\circ_{sn}(560nm)$, where $F_1 = 0.82$. The value of $p^\circ_{sn}(560$ nm) is referred to the solar noon and can be calculated for any day of the year, at any latitude between 60°S and 60°N. Interestingly, the equation for $\bar{p}_\circ(560$ nm) holds at all relevant latitudes and seasons.

- The coupling of CDOM absorption assessment with a global database of DOC values enables the mapping of [³CDOM*] on a quasi-global scale. The values of [³CDOM*] generally follow the daily doses of sunlight at the given latitudes and seasons. At the spring and fall equinoxes, however, where such doses vary less with latitude than in other times of the year, the usually high DOC values of lakes located in temperate areas of the northern hemisphere account for high [³CDOM*] values calculated for this region. Moreover, a combination of high DOC and high daily dose explains why the highest values of [³CDOM*] are predicted at 50–60°N during the summer solstice (June). The same does not happen in the southern hemisphere during

the winter solstice (December), because lake water in the relevant locations is characterized by relatively low values of the DOC.

- The [^{3}CDOM*] map is reflected into a map of photodegradation kinetics of compounds that mainly undergo transformation by reaction with ^{3}CDOM*. The case of clofibric acid (CLO) is considered here. Clear-sky CLO lifetimes of a couple of weeks or lower are predicted in many parts of the globe, in the 3-m uppermost layer of the global lakes.
- In many cases, photochemistry contributes to depollution. However, the ^{3}CDOM*-induced phototransformation of CLO into 4-chlorophenol and hydroquinone is likely to increase the ecological risk related to this contaminant.

Declaration of Competing Interest

The authors declare that they have no known competing financial interests or personal relationships that could have appeared to influence the work reported in this paper.

Data availability

Data will be made available on request.

Supplementary materials

Supplementary material associated with this article can be found, in the online version, at doi:10.1016/j.watres.2023.120153.

References

Avetta, P., Fabbri, D., Minella, M., Brigante, M., Maurino, V., Minero, C., Pazzi, M., Vione, D., 2016. Assessing the phototransformation of diclofenac, clofibric acid and naproxen in surface waters: model predictions and comparison with fi eld data. Water Res. 105, 383–394. https://doi.org/10.1016/j.watres.2016.08.058.
Bodrato, M., Vione, D., 2014. APEX (Aqueous Photochemistry of Environmentally occurring Xenobiotics): a free software tool to predict the kinetics of photochemical processes. Environ. Sci. Process. Impacts 16, 732–740. https://doi.org/10.1039/c3em00541k.
Braslavsky, S.E., 2007. Glossary of terms used in photochemistry 3rd edition. Pure Appl. Chem. 79, 293–465. https://doi.org/10.1351/pac200779030293.
Buth, J.M., Steen, P.O., Sueper, C., Blumentritt, D., Vikesland, P.J., Arnold, W.A., McNeill, K., 2010. Dioxin photoproducts of triclosan and its chlorinated derivatives in sediment cores. Environ. Sci. Technol. 44, 4545–4551. https://doi.org/10.1021/es1001105.
Buxton, G.V., Greenstock, C.L., Helman, P.W., Ross, A.B., 1988. Critical Review of rate constants for reactions of hydrated electrons, hydrogen atoms and hydroxyl radicals (·OH/·O−) in Aqueous Solution. J. Phys. Chem. Ref. Data 17, 513–886. https://doi.org/10.1063/1.555805.
Calza, P., Vione, D., 2015. Surface Water Photochemistry, Comprehensive Series in Photochemical & Photobiological Sciences, 297. The Royal Society of Chemistry. https://doi.org/10.1039/9781782622154.
Canonica, S., Jans, U., Stemmler, K., Hoigne, J., 1995. Transformation kinetics of phenols in water: photosensitization by dissolved natural organic material and aromatic ketones. Environ. Sci. Technol. 29, 1822–1831. https://doi.org/10.1021/es00007a020.
Canonica, S., Kohn, T., Mac, M., Real, F.J., Wirz, J., Von Gunten, U., 2005. Photosensitizer method to determine rate constants for the reaction of carbonate radical with organic compounds. Environ. Sci. Technol. 39, 9182–9188. https://doi.org/10.1021/es051236b.
Canonica, S., Laubscher, H.U., 2008. Inhibitory effect of dissolved organic matter on triplet-induced oxidation of aquatic contaminants. Photochem. Photobiol. Sci. 7, 547–551. https://doi.org/10.1039/b719982a.
Carena, L., Puscasu, C.G., Comis, S., Sarakha, M., Vione, D., 2019. Environmental photodegradation of emerging contaminants: a re-examination of the importance of triplet-sensitised processes, based on the use of 4-carboxybenzophenone as proxy for the chromophoric dissolved organic matter. Chemosphere 237, 124476. https://doi.org/10.1016/j.chemosphere.2019.124476.
Castiglioni, S., Zuccato, E., Fattore, E., Riva, F., Terzaghi, E., Koenig, R., Principi, P., Di Guardo, A., 2020. Micropollutants in Lake Como water in the context of circular economy: a snapshot of water cycle contamination in a changing pollution scenario. J. Hazard. Mater. 384, 121441 https://doi.org/10.1016/j.jhazmat.2019.121441.
Chen, Y., Hozalski, R.M., Olmanson, L.G., Page, B.P., Finlay, J.C., Brezonik, P.L., Arnold, W.A., 2020. Prediction of photochemically produced reactive intermediates in surface waters via satellite remote sensing. Environ. Sci. Technol. 54, 6671–6681. https://doi.org/10.1021/acs.est.0c00344.
Coimbra, A.M., Peixoto, M.J., Coelho, I., Lacerda, R., Carvalho, A.P., Gesto, M., Lyssimachou, A., Lima, D., Soares, J., André, A., Capitão, A., Castro, L.F.C., Santos, M.M., 2015. Chronic effects of clofibric acid in zebrafish (Danio rerio): a multigenerational study. Aquat. Toxicol. 160, 76–86. https://doi.org/10.1016/j.aquatox.2015.01.013.
Erickson, P.R., Grandbois, M., Arnold, W.A., McNeill, K., 2012. Photochemical formation of brominated dioxins and other products of concern from hydroxylated polybrominated diphenyl ethers (OH-PBDEs). Environ. Sci. Technol. 46, 8174–8180. https://doi.org/10.1021/es3016183.
Fenner, K., Canonica, S., Wackett, L.P., Elsner, M., 2013. Evaluating pesticide degradation in the environment: blind spots and emerging opportunities. Science (80-.) 341. https://doi.org/10.1126/science.1236281, 752 LP –758.
Finch, B.E., Marzooghi, S., Di Toro, D.M., Stubblefield, W.A., 2017. Phototoxic potential of undispersed and dispersed fresh and weathered Macondo crude oils to Gulf of Mexico marine organisms. Environ. Toxicol. Chem. 36, 2640–2650.
Frank, R., Klöpffer, W., 1988. Spectral solar photon irradiance in Central Europe and the adjacent North Sea. Chemosphere 17, 985–994. https://doi.org/10.1016/0045-6535(88)90069-0.
García-Gil, Á., Marugán, J., Vione, D., 2022. A model to predict the kinetics of direct (endogenous) virus inactivation by sunlight at different latitudes and seasons, based on the equivalent monochromatic wavelength approach. Water Res. 208, 117837 https://doi.org/10.1016/j.watres.2021.117837.
González-Ortegón, E., Giménez, L., Blasco, J., Le Vay, L., 2015. Effects of food limitation and pharmaceutical compounds on the larval development and morphology of Palaemon serratus. Sci. Total Environ. 503–504, 171–178. https://doi.org/10.1016/j.scitotenv.2014.08.118.
Gosset, A., Wiest, L., Fildier, A., Libert, C., Giroud, B., Hammada, M., Hervé, M., Sibeud, E., Vulliet, E., Polomé, P., Perrodin, Y., 2021. Ecotoxicological risk assessment of contaminants of emerging concern identified by "suspect screening" from urban wastewater treatment plant effluents at a territorial scale. Sci. Total Environ. 778, 146275 https://doi.org/10.1016/j.scitotenv.2021.146275.
Halladja, S., Amine-Khodja, A., ter Halle, A., Boulkamh, A., Richard, C., 2007. Photolysis of fluometuron in the presence of natural water constituents. Chemosphere 69, 1647–1654. https://doi.org/10.1016/j.chemosphere.2007.05.035.
Korkmaz, N.E., Savun-Hekimoğlu, B., Aksu, A., Burak, S., Caglar, N.B., 2022. Occurrence, sources and environmental risk assessment of pharmaceuticals in the Sea of Marmara, Turkey. Sci. Total Environ. 819, 152996 https://doi.org/10.1016/j.scitotenv.2022.152996.
Liu, G., Li, S., Song, K., Wang, X., Wen, Z., Kutser, T., Jacinthe, P.-A., Shang, Y., Lyu, L., Fang, C., Yang, Y., Yang, Q., Zhang, B., Cheng, S., Hou, J., 2021. Remote sensing of CDOM and DOC in alpine lakes across the Qinghai-Tibet Plateau using Sentinel-2A imagery data. J. Environ. Manage. 286, 112231 https://doi.org/10.1016/j.jenvman.2021.112231.
Mack, J., Bolton, J.R., 1999. Photochemistry of nitrite and nitrate in aqueous solution: a review. J. Photochem. Photobiol. A Chem. 128, 1–13. https://doi.org/10.1016/S1010-6030(99)00155-0.
Marchisio, A., Minella, M., Maurino, V., Minero, C., Vione, D., 2015. Photogeneration of reactive transient species upon irradiation of natural water samples: Formation quantum yields in different spectral intervals, and implications for the photochemistry of surface waters. Water Res. 73, 145–156. https://doi.org/10.1016/j.watres.2015.01.016.
McNeill, K., Canonica, S., 2016. Triplet state dissolved organic matter in aquatic photochemistry: reaction mechanisms, substrate scope, and photophysical properties. Environ. Sci. Process. Impacts 18, 1381–1399. https://doi.org/10.1039/C6EM00408C.
Messager, M.L., Lehner, B., Grill, G., Nedeva, I., Schmitt, O., 2016. Estimating the volume and age of water stored in global lakes using a geo-statistical approach. Nat. Commun. 7, 13603. https://doi.org/10.1038/ncomms13603.
National Renewable Energy Laboratory, Solar Position Algorithm| NREL. [WWW Document], 2022.
NCAR, 2015. Quick TUV calculator [WWW Document]. URL http://cprm.acom.ucar.edu/Models/TUV/Interactive_TUV/.
Niu, X.Z., Croué, J.P., 2019. Photochemical production of hydroxyl radical from algal organic matter. Water Res. 161, 11–16. https://doi.org/10.1016/j.watres.2019.05.089.
Ossola, R., Jönsson, O.M., Moor, K., McNeill, K., 2021. Singlet oxygen quantum yields in environmental waters. Chem. Rev. 121, 4100–4146. https://doi.org/10.1021/acs.chemrev.0c00781.

Packer, J.L., Werner, J.J., Latch, D.E., McNeill, K., Arnold, W.A., 2003. Photochemical fate of pharmaceuticals in the environment: naproxen, diclofenac, clofibric acid, and ibuprofen. Aquat. Sci. 65, 342–351. https://doi.org/10.1007/s00027-003-0671-8.

QGIS, 2020. QGIS Geographic information system. Open source geospatial foundation project.

Remucal, C.K., 2014. The role of indirect photochemical degradation in the environmental fate of pesticides: a review. Environ. Sci. Process. Impacts 16, 628–653. https://doi.org/10.1039/c3em00549f.

Sobek, S., Tranvik, L.J., Prairie, Y.T., Kortelainen, P., Cole, J.J., 2007. Patterns and regulation of dissolved organic carbon: an analysis of 7,500 widely distributed lakes. Limnol. Oceanogr. 52, 1208–1219. https://doi.org/10.4319/lo.2007.52.3.1208.

Sousa, J.C.G., Barbosa, M.O., Ribeiro, A.R.L., Ratola, N., Pereira, M.F.R., Silva, A.M.T., 2020. Distribution of micropollutants in estuarine and sea water along the Portuguese coast. Mar. Pollut. Bull. 154, 111120 https://doi.org/10.1016/j.marpolbul.2020.111120.

Sun, L., Qian, J., Blough, N.V., Mopper, K., 2015. Insights into the photoproduction sites of hydroxyl radicals by dissolved organic matter in natural waters. Environ. Sci. Technol. Lett. 2, 352–356. https://doi.org/10.1021/acs.estlett.5b00294.

Tixier, C., Singer, H.P., Oellers, S., Müller, S.R., 2003. Occurrence and fate of carbamazepine, clofibric acid, diclofenac, ibuprofen, ketoprofen, and naproxen in surface waters. Environ. Sci. Technol. 37, 1061–1068. https://doi.org/10.1021/es025834r.

Toming, K., Kotta, J., Uuemaa, E., Sobek, S., Kutser, T., Tranvik, L.J., 2020. Predicting lake dissolved organic carbon at a global scale. Sci. Rep. 10, 8471. https://doi.org/10.1038/s41598-020-65010-3.

Topaz, T., Boxall, A., Suari, Y., Egozi, R., Sade, T., Chefetz, B., 2020. Ecological risk dynamics of pharmaceuticals in micro-estuary environments. Environ. Sci. Technol. 54, 11182–11190. https://doi.org/10.1021/acs.est.0c02434.

Vione, D., Das, R., Rubertelli, F., Maurino, V., Minero, C., Barbati, S., Chiron, S., 2010. Modelling the occurrence and reactivity of hydroxyl radicals in surface waters: implications for the fate of selected pesticides. Intern. J. Environ. Anal. Chem. 90, 260–275.

Vione, D., 2021. The modelling of Surface-Water photoreactions made easier: introducing the concept of 'equivalent monochromatic wavelengths.' Water Res. 190, 116675. doi:10.1016/j.watres.2020.116675.

Vione, D., Carena, L., 2022. Direct photolysis of contaminants in surface freshwaters, within the equivalent monochromatic wavelength (EMW) approximation. Chemosphere 307, 135982. doi:10.1016/j.chemosphere.2022.135982.

Vione, D., Minella, M., Maurino, V., Minero, C., 2014. Indirect photochemistry in sunlit surface waters: photoinduced production of reactive transient species. Chem. Eur. J. 20, 10590–10606. https://doi.org/10.1002/chem.201400413.

Vogna, D., Marotta, R., Andreozzi, R., Napolitano, A., d'Ischia, M., 2004. Kinetic and chemical assessment of the UV/H2O2 treatment of antiepileptic drug carbamazepine. Chemosphere 54, 497–505. https://doi.org/10.1016/S0045-6535(03)00757-4.

Wenk, J., Canonica, S., 2012. Phenolic antioxidants inhibit the triplet-induced transformation of anilines and sulfonamide antibiotics in aqueous solution. Environ. Sci. Technol. 46, 5455–5462. https://doi.org/10.1021/es300485u.

Westerhoff, P., Mezyk, S.P., Cooper, W.J., Minakata, D., 2007. Electron pulse radiolysis determination of hydroxyl radical rate constants with suwannee river fulvic acid and other dissolved organic matter isolates. Environ. Sci. Technol. 41, 4640–4646. https://doi.org/10.1021/es062529n.

Wielens Becker, R., Ibáñez, M., Cuervo Lumbaque, .E.., Wilde, M.L., Flores da Rosa, T., Hernández, F., Sirtori, C., 2020. Investigation of pharmaceuticals and their metabolites in Brazilian hospital wastewater by LC-QTOF MS screening combined with a preliminary exposure and in silico risk assessment. Sci. Total Environ. 699, 134218 https://doi.org/10.1016/j.scitotenv.2019.134218.

Wojnárovits, L., Tóth, T., Takács, E., 2020. Rate constants of carbonate radical anion reactions with molecules of environmental interest in aqueous solution : a review. Sci. Total Environ. 717, 137219 https://doi.org/10.1016/j.scitotenv.2020.137219.

Yan, S., Liu, Y., Lian, L., Li, R., Ma, J., Zhou, H., Song, W., 2019. Photochemical formation of carbonate radical and its reaction with dissolved organic matters. Water Res. 161, 288–296. https://doi.org/10.1016/j.watres.2019.06.002.

Zhang, X., Lardizabal, A., Silverman, A.I., Vione, D., Kohn, T., Nguyen, T.H., Guest, J.S., 2020. Global sensitivity analysis of environmental, water quality, photoreactivity, and engineering design parameters in sunlight inactivation of viruses. Environ. Sci. Technol. 54, 8401–8410.

Zhang, T., Ma, H., Hong, Z., Fu, G., Zheng, Y., Li, Z., Cui, F., 2022. Photo-reactivity and photo-transformation of algal dissolved organic matter unraveled by optical spectroscopy and high-resolution mass spectrometry analysis. Environ. Sci. Technol. 56, 13439–13448.

Zhou, H., Lian, L., Yan, S., Song, W., 2017. Insights into the photo-induced formation of reactive intermediates from effluent organic matter: the role of chemical constituents. Water Res. 112, 120–128.